Journal of Materials Chemistry A

PAPER

View Article Online
View Journal | View Issue

Cite this: J. Mater. Chem. A, 2014, 2, 2256

Mesoporous magnetic carbon nanocomposite fabrics for highly efficient Cr(VI) removal†

Jiahua Zhu,‡[a] Hongbo Gu,[a] Jiang Guo,[ab] Minjiao Chen,[a] Huige Wei,[a] Zhiping Luo,[c] Henry A. Colorado,[d] Narendranath Yerra,[a] Daowei Ding,[a] Thomas C. Ho,[a] Neel Haldolaarachchige,[e] Jack Hopper,[a] David P. Young,[e] Zhanhu Guo*[a] and Suying Wei*[ab]

Received 1st October 2013
Accepted 28th October 2013

DOI: 10.1039/c3ta13957c

www.rsc.org/MaterialsA

We have demonstrated that magnetic carbon nanocomposite fabrics prepared by microwave assisted heating are advanced adsorbents in the removal of Cr(VI) with a much higher removal capacity of 3.74 mg g^{-1} compared to 0.32 mg g^{-1} for cotton fabrics and 0.46 mg g^{-1} for carbon fabrics. The enhanced Cr(VI) removal is attributed to the highly porous structure of the nanocomposites. The adsorption kinetics follow the pseudo-second-order model, which reveals a very large adsorption capacity and high adsorption rate. The removal process takes only 10 min, which is much faster than conventional adsorbents such as activated carbon and biomass that often requires hours of operation. The significantly reduced treatment time and the large adsorption capacity make these nanocomposite fabrics promising for the highly efficient removal of heavy metals from polluted water.

1. Introduction

With better awareness of the detrimental effects caused by Cr(VI) on the ecosystem, agriculture and human health[1–3] and its demanded usage in industrial fields such as leather tanning, electroplating, manufacturing of dyes, paints and paper,[4] technologies including cyanide treatment,[5] electro-chemical precipitation,[6] reverse osmosis (RO),[7,8] ion exchange (IE)[9,10] and adsorption[11–18] have been employed to remove Cr(VI) from polluted water. However, the maximum permissible level of 100 μg L^{-1} for the total Cr in drinking water, as recommended by the US Environmental Protection Agency (EPA),[19] has challenged these techniques. The World Health Organization and European Union designated an even lower provisional guideline value of 50 μg L^{-1} for the total Cr due to uncertainties in the toxicological database.[20] For example, the chlorination of cyanides can result in highly toxic intermediates and other toxic organochlorines. A large amount of precipitate sludge, arising from the precipitation technique, requires additional processes for further treatment. Though RO can effectively reduce the number of metal ions, its applications are limited by a number of disadvantages such as a high operational cost and limited pH range.[8] IE is a convenient method to treat the wastewater containing chromium ions, but only a limited amount of literature has reported the removal of Cr(III).[9,10,21] The operation cost is also higher than that of the other methods.[7] Though activated carbon is one of the most used adsorbents to purify polluted water,[22–24] it still fails to reduce the concentration of contaminants at ppb levels.[25] Iron minerals have been recognized as effective media for the removal of various heavy metals such as As(III) and As(V),[26] Cr(VI)[14] and Pd(II)[27] at very low concentrations. Iron and iron oxide nanostructures have proven to be efficient materials for heavy metal removal by reduction or adsorption.[28–30] Due to the difficulties in handling nanomaterials, researchers are trying to embed these functional nanostructures into a larger substrate. Therefore, the final hybrid materials can be easily handled while the nano-functionalities are maintained. Typically, carbon is often chosen as a substrate due to its low cost and high specific surface area.[31,32]

Methods to prepare carbon based nanocomposites include thermal decomposition,[33,34] self-assembly,[35,36] electrochemical deposition,[37,38] and the layer-by-layer technique.[39] All of these different methods allow better control of the nanostructures. However, they either have low efficiency for scale-up production

[a]Integrated Composites Laboratory (ICL), Dan F Smith Department of Chemical Engineering, Lamar University, Beaumont, TX 77710, USA. E-mail: zhanhu.guo@lamar.edu; suying.wei@lamar.edu; Tel: +1 (409) 880-7654; +1 (409) 880-7976

[b]Department of Chemistry and Biochemistry, Lamar University, Beaumont, TX 77710, USA

[c]Department of Chemistry and Physics and Southeastern North Carolina Regional Micro-analytical and Imaging Consortium, Fayetteville State University, Fayetteville, North Carolina 28301, USA

[d]Department of Mechanical and Aerospace Engineering, University of California Los Angeles, Los Angeles, CA 90095, USA

[e]Department of Physics and Astronomy, Louisiana State University, Baton Rouge, LA 70803, USA

† Electronic supplementary information (ESI) available: Further information about UV-Vis spectra and magnetic properties. See DOI: 10.1039/c3ta13957c

‡ Present address: Chemical and Biomolecular Engineering Department, The University of Akron, Akron, OH 44325, USA.

or require multiple skillful processes for successful synthesis. It is still a challenge to produce fibrous/porous carbon nanocomposites from a facile and economic process. Microwave synthesis using electromagnetic frequencies ranging from 0.3 to 300 GHz has been a promising technology for manufacturing nanomaterials with its extremely fast heating and cooling rates, which could not be achieved in a conventional heating process with a thermal diffusion controlled heating rate. In the microwave heating process, the average microwave power absorption value or the heating potential, depending on the dielectric properties of the material, frequency of the microwave, and the electric field intensity,[40–44] is given by eqn (1):

$$Q_{\text{avg}} = \omega\varepsilon_0\varepsilon'' {E_{\text{rms}}}^2 \quad (1)$$

where Q_{avg} is the average microwave power absorption or the heating potential in W m^{-3}, ω is the angular frequency in rad s^{-1}, ε_0 is the permittivity of free space (8.85×10^{-12} F m^{-1}), ε'' is the relative dielectric loss factor of the absorbing media, and E_{rms} is the electric field intensity in V m^{-1}. Throughout a given reaction, the reactants and intermediates can have different dielectric constants. Microwaves could selectively couple with the intermediate in the transition state and overcome the high activation energies for product formation.[45,46] The microwave heating reduces the overall thermal gradients in the reaction and thus yields more uniform products.[47–49] Various unique nanostructures have been synthesized using microwave energy, for example, core–shell Au–Pd bimetallic nanoparticles,[50] ZnS and ZnSe nanowires, CdSe nanorods,[51] $CoFe_2O_4$ nanoparticles,[52] Co_3O_4 rods,[53] and tellurium nanorods and nanowires.[54] Recently, we reported microwave assisted carbon–cobalt nanocomposites showing enhanced electrochemical energy storage compared to the nanocomposite counterpart from conventional tubular furnace heating[55] and magnetic carbon shell coated magnetic nanoparticles showing much better stability in acid etching[56] over the nanoparticles prepared under conventional tubular furnace annealing. However, a porous carbon nanocomposite manufactured using microwave energy has not been reported.

In this work, microtubular porous magnetic carbon nanocomposites were synthesized by conventional and microwave energy assisted annealing methods. Commercial T-shirt cotton fabric and iron nitrate served as carbon and iron precursors, which were converted to carbon fabric nanocomposites with doped metal/metal oxide nanostructures. The microstructure and magnetic properties of the nanocomposites were investigated by scanning electron microscopy (SEM), transmission electron microscopy (TEM), and a 9 T physical properties measurement system. The effects of the treatment time, initial Cr(VI) concentration, adsorbent loading and solution pH values on the Cr(VI) removal were investigated for the prepared carbon nanocomposites. The adsorption kinetics was also investigated by fitting the experimental data with suitable kinetic models. The carbon nanocomposites have been demonstrated to possess a very large removal capacity of Cr(VI) and an extremely fast removal rate.

2. Experimental

2.1. Materials preparation

Cotton fabric was cut from a commercially available T-Shirt. The inorganic salt, $Fe(NO_3)_3 \cdot 9H_2O$ (>98.0%), was purchased from Alfa Aesar. Three major steps were involved in the synthesis of the magnetic carbon nanocomposites. First, the cotton fabric (CottF) was dried at 80 °C in a regular oven for 6 hours; second, the dried CottF was cut into pieces (about 10 × 10 mm, total weight about 3 grams) and immersed in a beaker containing 40 mL of 1.0 M $Fe(NO_3)_3$ solution. After two hours, the beaker was moved to a vacuum oven and subjected to 700 mmHg vacuum for an additional 4 hours at room temperature. After that, the $Fe(NO_3)_3$ doped CottF was dried at 80 °C in a regular oven overnight; finally, the $Fe(NO_3)_3$ doped CottF was annealed to fabricate magnetic carbon nanocomposites. Two different annealing methods were used to compare the process-dependent material properties: (a) conventional annealing, the doped CottF fabrics were loaded in a tube furnace and heated to 850 °C with a heating rate of 10 °C min^{-1} in a N_2 atmosphere. The obtained product was named CN. Using 5% H_2–Ar mixture as the purging gas in a conventional process, the samples ignite immediately once exposed to air; (b) the doped CottF was annealed at ~850 °C using a microwave assisted heating system in 5% H_2–Ar and a high purity N_2 atmosphere for 2 hours and the resulting products were named MH and MN, respectively. For comparison, carbon fabrics (CarbF) were also fabricated by conventional annealing in a N_2 atmosphere. The detailed microwave annealing process is described in previous literature.[55,57]

2.2. Characterization

The morphology of the samples was characterized using scanning electron microscopy (SEM, Hitachi S-3400) and transmission electron microscopy (TEM, FEI Tecnai G2 F20) with a field emission gun, operated at an accelerating voltage of 200 kV. The TEM samples were prepared by drying a drop of sample–ethanol suspension on carbon-coated copper TEM grids.

The powder X-ray diffraction analysis of the samples was carried out with a Bruker AXS D8 Discover diffractometer with GADDS (General Area Detector Diffraction System) operating with a Cu-K α radiation source filtered with a graphite monochromator ($\lambda = 1.541$ Å).

The magnetic property measurements were carried out in a 9 T physical properties measurement system (PPMS) by Quantum Design at room temperature.

The specific Brunauer–Emmett–Teller (BET) surface areas and pore-size distributions were measured on a Quantachrome Nova 2200e by nitrogen adsorption at 77.4 K. Prior to each measurement, samples were degassed at 300 °C for 24 h under high vacuum (<0.01 mbar). The mesopore-size distribution was calculated by the Barrett–Joyner–Halenda (BJH) method using desorption isotherms.

The effects of the adsorbent concentration, the dichromate concentration and solution pH on the Cr(VI) removal percentage

(%) were studied. The experimental details have been given in ESI S1.†

3. Results and discussion

3.1. Microstructure investigation

Fig. 1 shows the SEM microstructure of the nanocomposite fibers after thermal treatment *via* the different processes. It shows that the fibers exhibit an average diameter of about 10–15 μm and the length can be easily extended to several centimeters without breakage, Fig. 1(a, c and e). The fibrous morphology was well maintained after the annealing process, which explains the excellent flexibility of the carbon nanocomposite fabrics. Taking a closer view on a single fiber of CN, Fig. 1(b), it is interesting to observe a hollow tube structure decorated with nanoparticles (white spots on the fiber) either on the fiber surface or within the fiber body matrix. This result confirms the successful conversion of the inorganic salt $Fe(NO_3)_3$ to nanoparticles as well as the conversion of the cotton to hollow carbon fibers. However, from the conventional annealing process, the nanoparticle size is not uniform and a significant amount of large particles were observed. Our previous study demonstrates that utilizing microwave energy in the annealing process helps to control the cobalt nanoparticle size and dispersion quality in a carbon matrix.[55] Therefore, microwave assisted annealing was also applied in the current study to fabricate uniformly sized iron nanoparticles. Both 5% H_2–Ar and N_2 were used as purging gases during the annealing and the properties of the products were comparatively investigated. Fig. 1(d) shows the microstructure of MH using microwave annealing in a 5% H_2–Ar atmosphere. The nanoparticle size and dispersion were well controlled as expected and no apparent agglomeration was observed, while the tube structure of the carbon fibers seems to have collapsed due to the twisting of the fibers during annealing. After replacing the purging gas with N_2, the surface of MN became much rougher with some debris adhering to the fiber, Fig. 1(e). Moreover, a highly porous structure was observed in MN, Fig. 1(f). This structure is very unique and a similar phenomenon has not been reported in previous literature. The most employed techniques for manufacturing porous carbon nanostructures mainly rely on the template method, either using hard[58,59] or soft templates.[60,61] However, the template approach usually suffers from high cost and complicated operations. In this work, a porous structure can be easily obtained without using any template. By simply applying microwave radiation, the $Fe(NO_3)_3$ doped CottF experienced a sharp temperature increase to about 850 °C, and carbonization occurred immediately once the temperature was increased. Volume shrinkage usually happened during carbonization, while the fiber structure was maintained, the shrinkage rate was much faster than the structure reorganization and thus a porous structure on the fibers was formed.

To determine the nanoparticle morphology in CN, MH, MN and their corresponding crystalline structures, HRTEM and SAED characterizations were conducted, Fig. 2. Fig. 2(a) shows the core–shell nanoparticle structure of CN. The measured lattice fringe spacing of 2.03 Å in the core area represents the

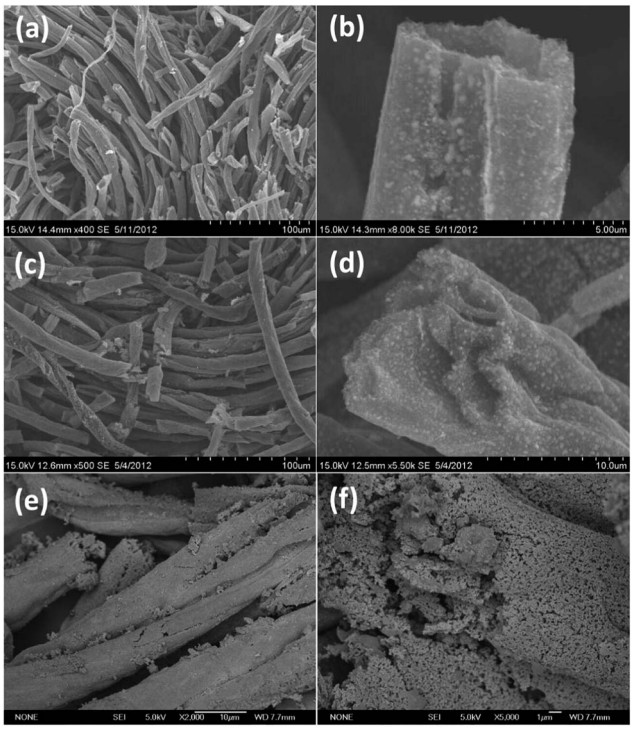

Fig. 1 SEM microstructures of (a & b) CN, (c & d) MH, and (e & f) MN.

crystalline plane of Fe (110) (PDF#06-0696). The carbon shell with a thickness of ~5 nm was observed with an obscure lattice structure. SAED provides more information on the crystalline structure of the nanoparticles, which includes the Fe crystal planes of (110, 200, 211, 220 and 310) (PDF#06-0696) and the Fe_2O_3 crystal plane of (311) (PDF#39-1346). Fig. 2(c) exhibits the core–shell structure of MH. Clear lattice fringes from both the core and shell areas are observed and were attributed to Fe (110) and Fe_2O_3 (311), respectively. A thin layer of graphitized carbon shell with a lattice fringe of 3.50 Å (002) was observed surrounding the core–shell nanoparticle. The SAED of the MH in Fig. 2(d) reveals more crystal planes of Fe (200, 220 and 310). In MN, the nanoparticle core–shell structure becomes less obvious, Fig. 2(e). From the lattice fringe HRTEM, only Fe_2O_3 (311) and C (002) could be identified and the SAED in Fig. 2(f) illustrates the existence of Fe (110) and Fe (220) crystalline planes. Since HRTEM and SAED only provide crystalline information focusing on very small areas, XRD characterization was conducted to reveal the crystalline information in bulk, Fig. 3. Comparing the XRD profiles of CN and MH/MN, the particles in CN have been heavily oxidized to Fe_2O_3 and most of the oxide crystalline peaks are observed, Fig. 3(a). In MH and MN, fewer oxide peaks were observed indicating that the as-synthesized nanoparticles were better protected from oxidation by the graphitized carbon shell.

Specific surface area and pore size determination of the carbon and nanocomposite fabrics is critically important since their surface properties dominate the interfacial behavior when they are used as adsorbents. Fig. 4 shows the nitrogen adsorption–desorption isotherms of the CarbF (Fig. 4(a)) and nanocomposites

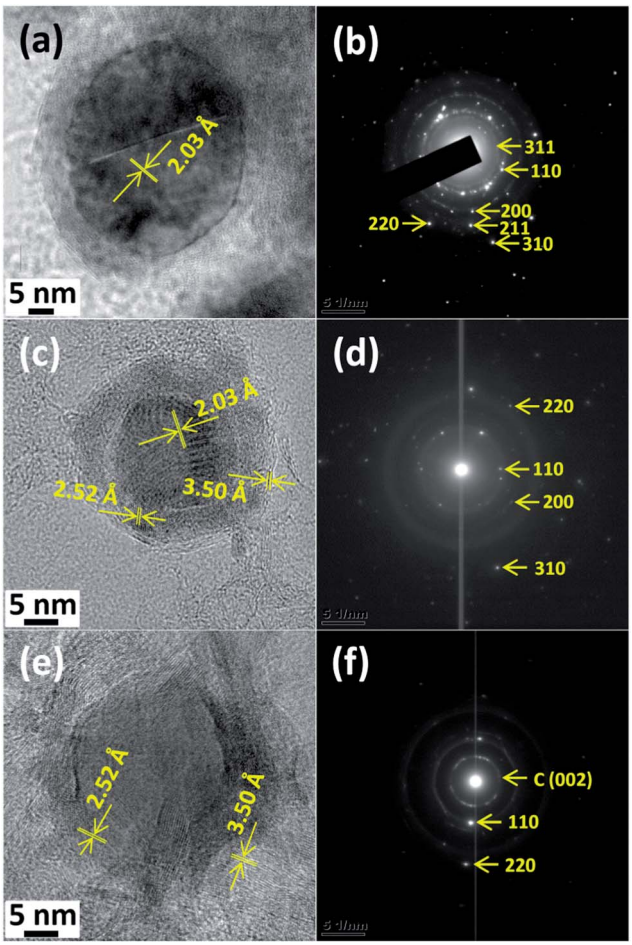

Fig. 2 HRTEM images of (a) CN, (c) MH, (e) MN and their corresponding selected area electron diffraction (SAED) patterns (b), (d) and (f), respectively.

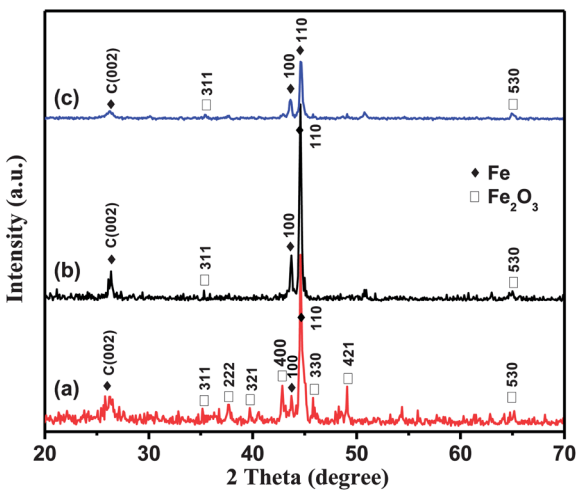

Fig. 3 XRD profiles of (a) CN, (b) MH, and (c) MN.

(Fig. 4(b–d)), which clearly show the representative type-IV curves.[62,63] The BJH pore size distribution curves calculated from the desorption branches are presented in Fig. 5(a–d), respectively.

It is clearly shown that the pore radius size of all samples is centered at ~20 Å with a narrow size distribution, indicating their characteristic diameter of ~40 Å in the mesoporous range of 20–500 Å. The CarbF shows the highest specific surface area of 295.9 $m^2\ g^{-1}$ with a pore volume of 0.16 $cm^3\ g^{-1}$. The nanocomposites exhibit an obviously decreased specific surface area, for example, CN (190.1 $m^2\ g^{-1}$), MH (91.1 $m^2\ g^{-1}$) and MN (73.7 $m^2\ g^{-1}$). One of the major reasons for the decreased specific surface area in the nanocomposites is that the nanoparticles with the larger density put extra weight on the composites, which results in a decrease in the surface area per unit weight even if the absolute surface area remains the same. In addition, the absolute surface area of the nanocomposite may also decrease due to the "blocking" effect of the nanoparticles within the porous carbon. The nanoparticles could either fill in the pore space to occupy the effective surface area or block partial channels to seal the channel space. After examining the pore volume of each nanocomposite, it is found that the nanocomposites, CN (0.26 $cm^3\ g^{-1}$), MH (0.16 $cm^3\ g^{-1}$) and MN (0.15 $cm^3\ g^{-1}$), show comparable or even larger pore volumes than that of CarbF. In other words, the "blocking" effect of the nanoparticles is negligible in the nanocomposites. Taking the extra weight of the nanoparticles into consideration, the real pore volume of the nanocomposites is actually larger than that of CarbF. The incorporation of the nanoparticles in the porous carbon helps to create extra pore volume space. This phenomenon could be interpreted by the "catalytic" effect of iron nanoparticles. During annealing, the doped iron nitrate salt was first decomposed to iron nuclei at a relatively low temperature of less than 400 °C.[64] These nuclei migrated under elevated temperatures and formed catalytically active nanoparticles for carbon graphitization.[65] The graphitized carbon compactly aligned, surrounding the spherical nanoparticles and leaving void space between individual particles. Therefore, extra pore volume was created after incorporating the nanoparticles. The schematic formation mechanism of the nanocomposites and the creation of the extra pore volume within the nanocomposites is illustrated in Scheme 1.

3.2. Chromium removal by magnetic nanocomposites

To quantify the Cr(VI) concentration in solution, a linear standard curve relating the UV-Vis peak intensity at 540 nm and Cr(VI) concentration has been made, Fig. S3.† The residual Cr(VI) concentration after treatment can be calculated from the standard curve. To evaluate the efficiency of different adsorbents, removal percentage (RP, %) is introduced as a criterion which can be calculated using eqn (2).

$$\mathrm{RP} = \frac{C_0 - C_r}{C_0} \times 100\% \qquad (2)$$

where C_0 is the initial concentration of the Cr(VI) solution and C_r represents the remaining Cr(VI) concentration after treatment. The obtained CN, MH and MN were used as adsorbents to remove the Cr(VI) from pre-prepared Cr(VI) aqueous solution. Cr(VI) removal with CottF and CarbF (manufactured from cotton fabric by conventional annealing) was also investigated for comparison.

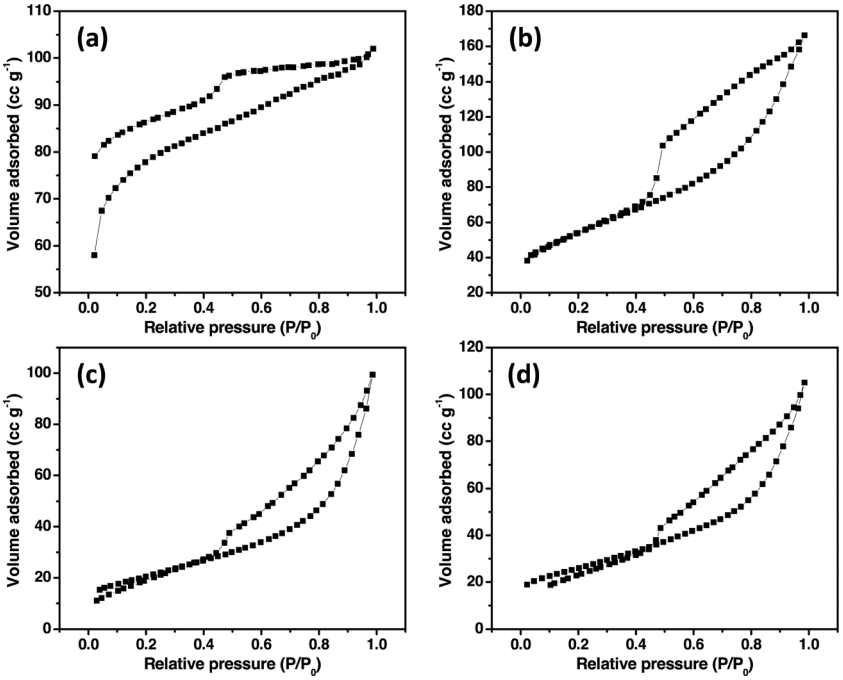

Fig. 4 Nitrogen isotherms of (a) CarbF, (b) CN, (c) MH and (d) MN at 77.4 K.

Fig. 6 shows the RP of the different adsorbents in neutral solution. The adsorbent concentration was maintained at a constant value of 1.0 g L^{-1} and a short contact time of 10 min was employed in this study. Both MH and MN show complete Cr(VI) removal with an initial concentration of 1.5 mg L^{-1}, while CN only shows 68.7% RP and even lower values are reported for CottF (21.3%) and CarbF (30.7%). This result reveals the superior performance for Cr(VI) removal of MH and MN over CottF, CarbF and CN. However, the result is not able to determine the specific removal capacity of MH and MN, since both of them achieve complete removal of the Cr(VI). MH and MN were further tested in a Cr(VI) solution of a higher concentration of 4.0 mg L^{-1} and the results are shown in Fig. 6. It is obvious that the RP of MN (88.9%) is relatively higher than that of MH

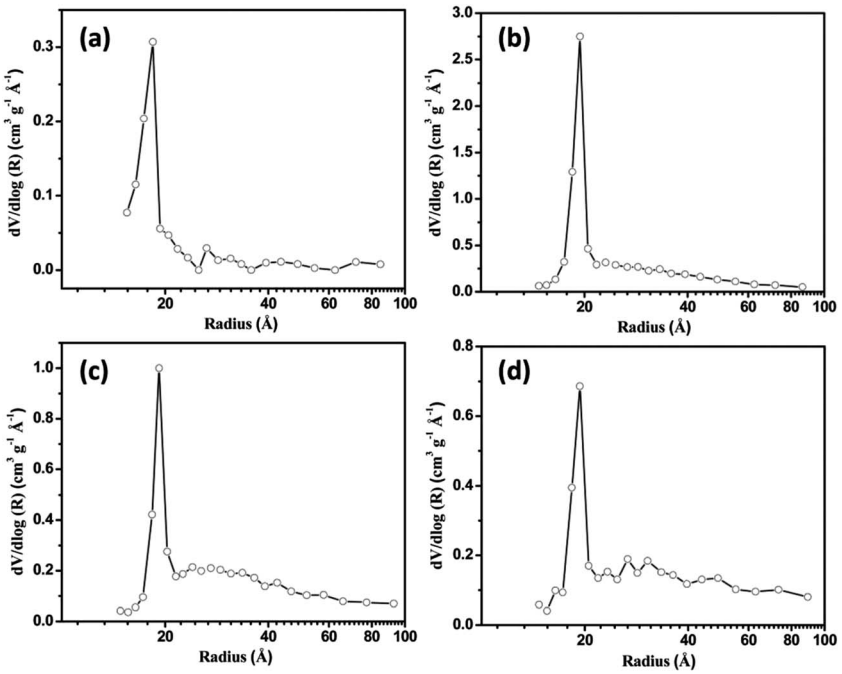

Fig. 5 Pore size distribution of (a) CarbF, (b) CN, (c) MH and (d) MN calculated using the BJH method.

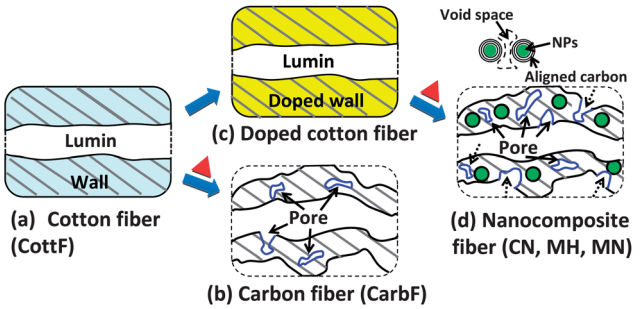

Scheme 1 (a) Hollow structure of cotton fibers with fiber wall and lumin, (b) porous structure of carbon fiber after annealing at 800 °C, (c) iron nitrate doped cotton fabric, (d) nanocomposite fibers doped with nanoparticles and some extra pores have been created as marked by the dash arrow.

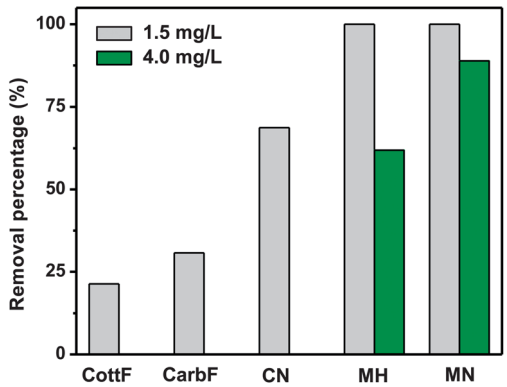

Fig. 6 The Cr(VI) removal performance of different materials. [Adsorbent] = 1.0 g L^{-1}, treatment time: 10 min, solution pH = 7. For UV-Vis spectra refer to ESI Fig. S1 and S2.†

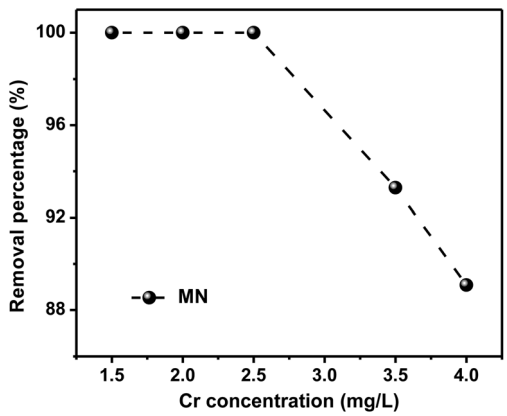

Fig. 7 Cr(VI) RP from solutions of different concentrations. [MN] = 1.0 g L^{-1}, treatment time: 10 min, solution pH = 7. For UV-Vis spectra refer to ESI Fig. S4.†

(61.9%). Therefore, MN will be used as the model compound to systematically study the Cr removal kinetics and mechanisms. The MN exhibits the lowest specific surface area and pore volume among all of the samples, which has been evidenced by

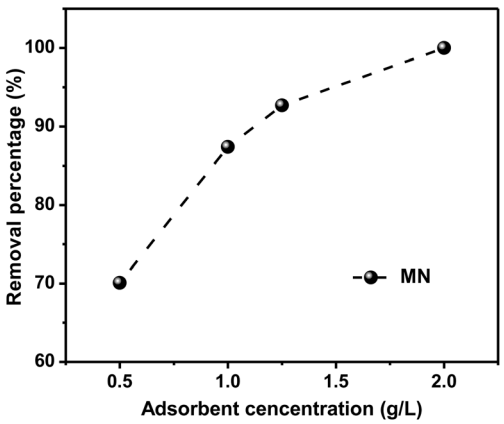

Fig. 8 Cr(VI) removal percentage with different MN concentrations. [Cr(VI)] = 4.0 mg L^{-1}, treatment time: 10 min, solution pH = 7. For UV-Vis spectra refer to ESI Fig. S5.†

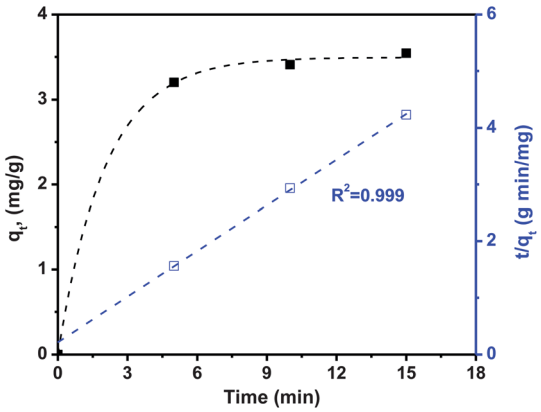

Fig. 9 Kinetic adsorption data plots of Cr(VI) adsorption by MN: Cr(VI) removal rate q_t *vs.* time t (solid square) and the transformed rate plot t/q_t *vs.* t (open square). [MN] = 1 g L^{-1}, [Cr(VI)] = 4.0 mg L^{-1}, pH = 7. For UV-Vis spectra refer to ESI Fig. S6.†

the BET results in Fig. 4 and 5. In other words, the specific surface area and pore volume are not the dominant factors determining the ability of the nanocomposites to remove Cr(VI) from water. The surface properties of the embedded nanoparticles play a more important role and the mechanisms will be discussed in the following section. With a very short treatment time of 10 min, the removal capacity of MN reaches 3.56 mg g^{-1}, which is much higher than those of previously reported carbon nanocomposites (1.03 mg g^{-1})[33] and other nanoparticles (0.3–2.4 mg g^{-1}).[66]

The effect of the initial Cr(VI) concentration on the removal efficiency of MN in a neutral solution is shown in Fig. 7. The MN concentration was maintained at a constant value of 1.0 g L^{-1} and a short contact time of 10 min was employed in this study. A maximum RP of 100% was achieved for the initial Cr(VI) concentrations of 1.5, 2.0 and 2.5 mg L^{-1}. Thereafter, the RP decreased on increasing the initial Cr(VI) concentration. This is because the MN sites eventually become saturated with adsorbed Cr(VI), at which point further addition of Cr(VI) to the

Table 1 Comparison of adsorption capacity and rate constant with other materials

Materials	Adsorption capacity (mg g^{-1})	Adsorption rate constant (g mg^{-1} min^{-1})	Ref.
MN (in this work)	3.74	0.30	
Aluminum–magnesium mixed hydroxide	105.3–112.0[a]	<0.024	72
Pomegranate husk carbon	35.2[b]	<0.032	73
Activated carbon	112.36[c]	<0.093	74
Carbon coated magnetic nanoparticles	1.52	0.099	34
Agricultural waste biomass	0.28–0.82	N/A	75
Graphene nanocomposites	1.03	0.28	33
Commercial α-Fe_2O_3	0.68	N/A	76
Commercial CeO_2	0.37	N/A	66
3D flower-like CeO_2	5.9	N/A	66

[a] The large adsorption capacity of aluminum–magnesium mixed hydroxide is due to the ion exchange mechanism rather than adsorption which results in the very low adsorption rate. [b] Pomegranate husk carbon. [c] Activated carbon exhibits a very high specific adsorption capacity due to their extremely low densities. Nanocomposites with metal oxides have significantly higher densities. Therefore, the specific adsorption capacity based on unit mass is much lower.

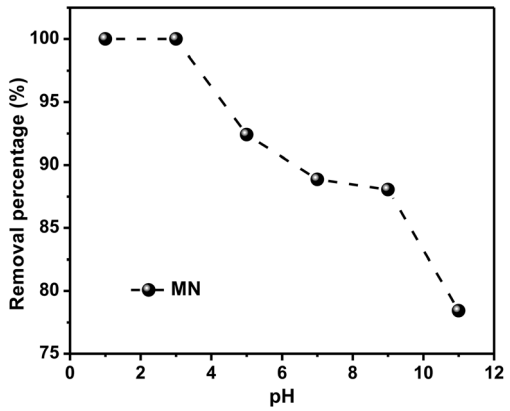

Fig. 10 Effect of solution pH on the Cr(VI) removal efficiency of MN. [MN] = 1.0 g L^{-1}, [Cr(VI)] = 4.0 mg L^{-1}, treatment time: 10 min. For UV-Vis spectra refer to ESI Fig. S7.†

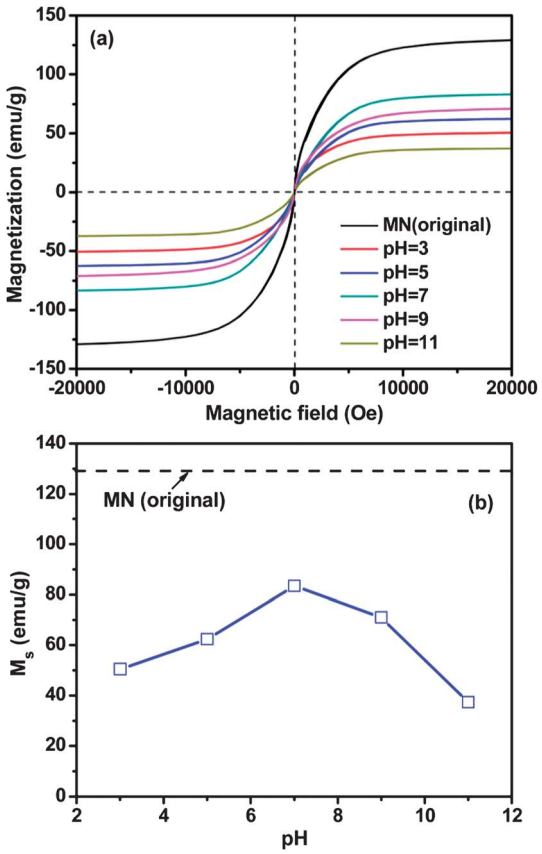

Fig. 11 (a) Magnetic hysteresis loop of MN (original) and MN after treatment in Cr(VI) solutions of different pH values. (b) Magnetization as a function of the solution pH (the dashed line indicates the magnetization of the original MN).

solution hardly increases the amount of adsorbed Cr(VI) significantly. Keeping the highest Cr(VI) concentration of 4.0 mg L^{-1} with the same contact time of 10 min, different loadings of MN are applied to investigate the Cr(VI) removal performance, Fig. 8. It is observed that the RP increases on increasing the MN loading due to the increased number of adsorption sites with the larger amount of MN. The maximum RP of ~100% could be achieved with an MN loading of 2.0 g L^{-1}.

The kinetics of the adsorption that describes the Cr(VI) uptake rate is a characteristic that controls the residence time of the adsorbate uptake at the solid/solution interface. In the present study, two continuous processes occurred during the entire removal process. Firstly, the Cr(VI) ions start to diffuse into the porous carbon channel once they contact the adsorbent surface. Some of the ions are adsorbed on the carbon surface and the others are transported further to the magnetic nanoparticle surface, where a redox reaction occurs immediately to reduce the Cr(VI) to less toxic Cr(III). The redox reaction process is much faster than the diffusion process. Therefore, the diffusion step dominates the removal efficiency in terms of adsorption rate. Here, the kinetics of the Cr(VI) removal was carried out to understand the diffusion/adsorption behavior of Cr(VI) on the MN. Fig. 9 shows the adsorption data of Cr(VI) over MN at different time intervals of 5, 10 and 15 minutes. Different

kinetics models including pseudo-first-order,[67] pseudo-second-order,[68] Elovich[69,70] and intraparticle diffusion[71] have been used to fit the experimental results and the correlation coefficient (R^2) is introduced to evaluate the suitability of the different models. The higher R^2 value indicates a more applicable model to the Cr(VI) adsorption kinetics. Among these models, pseudo-second order obtains the highest correlation coefficient of $R^2 = 0.999$ (fitting curve is shown in Fig. 9, open square curve), which can be expressed in eqn (3):

$$\frac{t}{q_t} = \frac{1}{k_{ad} q_e^2} + \frac{t}{q_e} \quad (3)$$

where q_t (mg g^{-1}) is the solid-phase loading of Cr(VI) in the MN at time t (min), q_e (mg g^{-1}) is the adsorption capacity at equilibrium, k_{ad} (g mg^{-1} min^{-1}) is the rate constant of adsorption and h (mg g^{-1} min^{-1}) is the initial adsorption rate at t approaching zero, $h = k_{ad} q_e^2$. The adsorption capacities and adsorption rate constants have been summarized and compared with other reported materials in Table 1.

The solution pH is one of the most important variables affecting the adsorption characteristics. The Cr(VI) removal efficiency of the MN in solutions of different pH is shown in Fig. 10 with an initial Cr(VI) concentration of 4.0 mg L^{-1} and an MN concentration of 1.0 g L^{-1}. At a fixed adsorbent concentration, complete Cr(VI) removal was achieved under acidic conditions when the pH was controlled at 1 and 3. Increasing the solution pH to 5 and even higher, the RP decreases gradually to 88.1% at pH = 9. At the solution pH of 11, the RP sharply decreases to 78.4%. However, this pH dependent performance of MN is much better than the previously reported result of 5% RP (at pH = 11) on porous carbon coated magnetic nanoparticles.[34] Cr(VI) exists in different ionic forms depending on the solution pH and total chromate concentration.[49,50] Chromate (CrO_4^{2-}), dichromate ($Cr_2O_7^{2-}$) and hydrogen chromate ($HCrO_4^-$) are the most recognized Cr(VI) ion forms in solution.[72,77] At a pH lower than 6.8, $HCrO_4^-$ is the dominant species and above 6.8 only CrO_4^{2-} is stable. The dependence of the Cr(VI) removal on the solution pH can be explained from the perspective of the surface chemistry at the interface. At low pH, the large amount of protons on the MN surface helps to adsorb the Cr(VI) species and therefore a higher RP is achieved. With an increase in pH, the uptake of the Cr(VI) ions decreases, which is due to the higher concentration of OH^- ions present in the solution that compete with the Cr(VI) species on the MN surface.

3.3. Chromium removal mechanisms

All of the synthesized nanocomposites show strong magnetization either from the conventional or microwave assisted annealing process. The CN and MH exhibit a large saturation magnetization of ~100 emu g^{-1}, Fig. S8† and low coercivities of 97.4 Oe and 73.7 Oe, respectively (inset of Fig. S8†). MN shows an even larger saturation magnetization of 130 emu g^{-1} and negligible coercivity, Fig. 11. The large saturation magnetization and small coercivity indicate the superparamagnetic property of all of these nanocomposites. The strong magnetization allows their facile magnetic separation using a permanent magnet after treatment, which is industrially desirable due to the economic and energy-saving separation process. More importantly, the material component change during the treatment can be monitored by the change in magnetization, which would explain further the Cr(VI) removal mechanism. Once the redox reaction occurs between the Cr(VI) and the iron/iron oxide nanoparticles following the reactions indicated below (4–6), the magnetization of the nanocomposites decreases due to the lower saturated magnetization of iron oxides (FeO: 47.4 emu g^{-1};[78] α-Fe_2O_3: 1.2 emu g^{-1} at 10 000 Oe;[79] γ-Fe_2O_3: 64.0 emu g^{-1};[80]) than that of pure iron (218.0 emu g^{-1};[81]):

$$Fe^0 + Cr(VI) \rightarrow Fe^{2+} + Cr(III) \quad (4)$$

$$Fe^0 + H_2O \rightarrow Fe^{2+} + OH^- + H_2 \quad (5)$$

$$Fe^{2+} + Cr(VI) \rightarrow Fe^{3+} + Cr(III) \quad (6)$$

Fig. 11(a) shows the magnetic hysteresis loops of MN and MN after treatment in solutions of different pH. The saturation magnetization of each curve is summarized in Fig. 11(b). It is obvious that the saturation magnetization of MN at each pH condition decreases significantly after the treatment process. The loss of magnetization in acidic or basic solutions is even more serious than that in neutral solutions. In low pH solutions, the protons provide positive charge to adsorb the $HCrO_4^-$ and thus a high removal percentage is observed. Besides the adsorption, the redox reaction also occurred at the interface of the magnetic nanoparticles and the Cr(VI) species, which has been well studied in previous literature.[82,83] The redox reaction proceeds faster in acidic solutions due to the dissolution of nanoparticles as revealed by the loss of magnetization, which explains the larger loss of magnetization in low pH solutions, Fig. 11(b). In basic solutions, the loss of magnetization of nanoparticles is mainly due to oxidation rather than dissolution.

4. Conclusion

Starting from the cost effective precursors of cotton fabrics and the iron nitrate inorganic salt, mesoporous nanocomposite fabrics were manufactured from both conventional and microwave assisted annealing processes for highly efficient Cr(VI) removal from polluted water. Magnetic carbon nanocomposites showing hollow fiber, distorted tube and porous fiber structures can be obtained by selecting the annealing method (conventional or microwave) and purging gas species (5% H_2–Ar or N_2). These carbon nanocomposite fabrics show a much higher Cr(VI) removal capacity than those of cotton and carbon fabrics and the removal kinetics follow a pseudo-second-order behavior. A high Cr(VI) removal capacity of 3.74 mg g^{-1} has been achieved in neutral solution. Even higher removal capacitance is observed in lower pH solutions. Complete Cr(VI) removal within only 10 min is much faster than other previously reported materials, such as carbon,[84] waste biomass[75] and lignocellulosic substrate,[85] which often require hours or even

days of treatment and still the Cr(VI) cannot be removed completely. These carbon nanocomposite fabrics show great potential in polluted water treatment in terms of their low manufacturing cost, simple processing and high removal efficiency of heavy metals.

Acknowledgements

The support from National Science Foundation-Nanoscale Interdisciplinary Research Team and Materials Processing and Manufacturing (CMMI 10-30755) is kindly acknowledged. This work is partially supported by the seeded Research Enhancement Grant (REG) of Lamar University and Texas Hazardous Waste Research Center (THWRC). DPY acknowledges support from the NSF under grant DMR 13-06392.

References

1 P. Battistoni, G. Fava and M. L. Ruello, *Water Res.*, 1993, **27**, 821–827.
2 H. Schat, S. S. Sharma and R. Vooijs, *Physiol. Plant.*, 1997, **101**, 477–482.
3 L. C. Hsu, S. L. Wang, Y. C. Lin, M. K. Wang, P. N. Chiang, J. C. Liu, W. H. Kuan, C. C. Chen and Y. M. Tzou, *Environ. Sci. Technol.*, 2010, **44**, 6202–6208.
4 A. Agrawal, V. Kumar and B. D. Pandey, *Miner. Process. Extr. Metall. Rev.*, 2006, **27**, 99–130.
5 L. Monser and N. Adhoum, *Sep. Purif. Technol.*, 2002, **26**, 137–146.
6 N. Kongsricharoern and C. Polprasert, *Water Sci. Technol.*, 1996, **34**, 109–116.
7 A. Hafez and S. El-Mariharawy, *Desalination*, 2004, **165**, 141–151.
8 Z. Modrzejewska and W. Kaminski, *Ind. Eng. Chem. Res.*, 1999, **38**, 4946–4950.
9 S. Rengaraj, C. K. Joo, Y. Kim and J. Yi, *J. Hazard. Mater.*, 2003, **102**, 257–275.
10 S. Rengaraj, K.-H. Yeon and S.-H. Moon, *J. Hazard. Mater.*, 2001, **87**, 273–287.
11 (*a*) D. Zhang, S. Wei, C. Kaila, X. Su, J. Wu, A. B. Karki, D. P. Young and Z. Guo, *Nanoscale*, 2010, **2**, 917–919; (*b*) H. Gu, S. Rapole, J. Sharma, Y. Huang, D. Cao, H. Colorado, Z. Luo, N. Haldolaarachchige, D. P. Young, B. Walters, S. Wei and Z. Guo, *RSC Adv.*, 2012, **2**, 11007–11018; (*c*) H. Gu, S. Rapole, Y. Huang, D. Cao, Z. Luo, S. Wei and Z. Guo, *J. Mater. Chem. A*, 2013, **1**, 2011–2021.
12 D. Mohan, K. P. Singh and V. K. Singh, *Ind. Eng. Chem. Res.*, 2005, **44**, 1027.
13 Y. C. Sharma, B. Singh, A. Agrawal and C. H. Weng, *J. Hazard. Mater.*, 2008, **151**, 789–793.
14 J. Hu, G. Chen and I. M. C. Lo, *Water Res.*, 2005, **39**, 4528–4536.
15 (*a*) Y. A. AydIn and N. D. Aksoy, *Chem. Eng. J.*, 2009, **151**, 188–194; (*b*) J. Zhu, M. Chen, Q. He, L. Shao, S. Wei and Z. Guo, *RSC Adv.*, 2013, **3**, 22790.
16 Y. Zhao, J. R. Peralta-Videa, M. L. Lopez-Moreno, M. Ren, G. Saupe and J. L. Gardea-Torresdey, *Environ. Sci. Technol.*, 2011, **45**, 1082–1087.
17 M. F. Sawalha, J. L. Gardea-Torresdey, J. G. Parsons, G. Saupe and J. R. Peralta-Videa, *Microchem. J.*, 2005, **81**, 122–132.
18 J. G. Parsons, M. Hejazi, K. J. Tiemann, J. Henning and J. L. Gardea-Torresdey, *Microchem. J.*, 2002, **71**, 211–219.
19 Y. Xu and D. Zhao, *Water Res.*, 2007, **41**, 2101–2108.
20 *Guidelines for drinking-water quality. Health criteria and other supporting information*, World Health Organization, vol. 2, 2nd edn, 1996.
21 M. Pansini, C. Colella and M. De Gennaro, *Desalination*, 1991, **83**, 145–157.
22 M. A. A. Zaini, R. Okayama and M. Machida, *J. Hazard. Mater.*, 2009, **170**, 1119–1124.
23 S.-Y. Wang, M.-H. Tsai, S.-F. Lo and M.-J. Tsai, *Bioresour. Technol.*, 2008, **99**, 7027–7033.
24 Z. Tu, Q. He, X. Chang, Z. Hu, R. Gao, L. Zhang and Z. Li, *Anal. Chim. Acta*, 2009, **649**, 252–257.
25 K. Pillay, E. M. Cukrowska and N. J. Coville, *J. Hazard. Mater.*, 2009, **166**, 1067–1075.
26 V. Chandra, J. Park, Y. Chun, J. W. Lee, I.-C. Hwang and K. S. Kim, *ACS Nano*, 2010, **4**, 3979–3986.
27 S. Shin and J. Jang, *Chem. Commun.*, 2007, 4230–4232.
28 W.-x. Zhang, *J. Nanopart. Res.*, 2003, **5**, 323–332.
29 S. M. Ponder, J. G. Darab and T. E. Mallouk, *Environ. Sci. Technol.*, 2000, **34**, 2564–2569.
30 J.-S. Hu, L.-S. Zhong, W.-G. Song and L.-J. Wan, *Adv. Mater.*, 2008, **20**, 2977–2982.
31 L. C. A. Oliveira, R. V. R. A. Rios, J. D. Fabris, V. Garg, K. Sapag and R. M. Lago, *Carbon*, 2002, **40**, 2177–2183.
32 (*a*) R. L. Vaughan Jr and B. E. Reed, *Water Res.*, 2005, **39**, 1005–1014; (*b*) S. Wei, Q. Wang, J. Zhu, L. Sun, H. Lin and Z. Guo, *Nanoscale*, 2011, **3**, 4474–4502.
33 J. Zhu, S. Wei, H. Gu, S. B. Rapole, Q. Wang, Z. Luo, N. Haldolaarachchige, D. P. Young and Z. Guo, *Environ. Sci. Technol.*, 2012, **46**, 977–985.
34 J. Zhu, H. Gu, S. B. Rapole, Z. Luo, S. Pallavkar, N. Haldolaarachchige, T. J. Benson, T. C. Ho, J. Hopper, D. P. Young, S. Wei and Z. Guo, *RSC Adv.*, 2012, **2**, 4844–4856.
35 J. Li, S. Tang, L. Lu and H. C. Zeng, *J. Am. Chem. Soc.*, 2007, **129**, 9401–9409.
36 D. Wang, R. Kou, D. Choi, Z. Yang, Z. Nie, J. Li, L. V. Saraf, D. Hu, J. Zhang, G. L. Graff, J. Liu, M. A. Pope and I. A. Aksay, *ACS Nano*, 2010, **4**, 1587–1595.
37 E. S. Steigerwalt, G. A. Deluga and C. M. Lukehart, *J. Phys. Chem. B*, 2002, **106**, 760–766.
38 J. Yan, H. Zhou, P. Yu, L. Su and L. Mao, *Electrochem. Commun.*, 2008, **10**, 761–765.
39 N. Du, H. Zhang, B. D. Chen, X. Y. Ma, Z. H. Liu, J. B. Wu and D. R. Yang, *Adv. Mater.*, 2007, **19**, 1641–1645.
40 I. Plazl, G. Pipus and T. Koloini, *AIChE J.*, 1997, **43**, 754–760.
41 Industrial Microwave Heating, *Power Engineering Series 4*, ed. A. C. Metaxas and R. J. Meredith, London, UK, 1983.
42 Z. Hashisho, M. Rood and L. Botich, *Environ. Sci. Technol.*, 2005, **39**, 6851–6859.

43 M. D. Turner, R. L. Laurence, W. C. Conner and K. S. Yngvesson, *AIChE J.*, 2000, **46**, 758–768.
44 T. Ohgushi, Y. Sakai, Y. Adachi and H. Satoh, *J. Phys. Chem. C*, 2009, **113**, 8206–8210.
45 *Microwaves in Organic Synthesis*, ed. A. Loupy, Wiley-VCH, Weinheim, Germany and Cambridge, UK, 2002.
46 J. A. Gerbec, D. Magana, A. Washington and G. F. Strouse, *J. Am. Chem. Soc.*, 2005, **127**, 15791–15800.
47 W. X. Chen, J. Y. Lee and Z. Liu, *Chem. Commun.*, 2002, 2588–2589.
48 B. Hu, S.-B. Wang, K. Wang, M. Zhang and S.-H. Yu, *J. Phys. Chem. C*, 2008, **112**, 11169–11174.
49 P. Raveendran, J. Fu and S. L. Wallen, *Green Chem.*, 2006, **8**, 34–38.
50 R. Harpeness and A. Gedanken, *Langmuir*, 2004, **20**, 3431–3434.
51 A. B. Panda, G. Glaspell and M. S. El-Shall, *J. Am. Chem. Soc.*, 2006, **128**, 2790–2791.
52 F. Bensebaa, F. Zavaliche, P. L'Ecuyer, R. W. Cochrane and T. Veres, *J. Colloid Interface Sci.*, 2004, **277**, 104–110.
53 W.-W. Wang and Y.-J. Zhu, *Mater. Res. Bull.*, 2005, **40**, 1929–1935.
54 Y.-J. Zhu, W.-W. Wang, R.-J. Qi and X.-L. Hu, *Angew. Chem.*, 2004, **116**, 1434–1438.
55 J. Zhu, M. Chen, N. Yerra, N. Haldolaarachchige, S. Pallavkar, Z. Luo, T. C. Ho, J. Hopper, D. P. Young, S. Wei and Z. Guo, *Nanoscale*, 2013, **5**, 1825–1830.
56 H. Gu, D. Ding, P. Sameer, J. Guo, N. Yerra, Y. Huang, Z. Luo, T. C. Ho, N. Halolaarachchige, D. P. Young, A. Kasanov, Z. Guo and S. Wei, *ECS Solid State Lett.*, 2013, **3**, M65–M68.
57 J. Zhu, S. Pallavkar, M. Chen, N. Yerra, Z. Luo, H. A. Colorado, H. Lin, N. Haldolaarachchige, A. Khasanov, T. C. Ho, D. P. Young, S. Wei and Z. Guo, *Chem. Commun.*, 2013, **49**, 258–260.
58 S. A. Johnson, E. S. Brigham, P. J. Ollivier and T. E. Mallouk, *Chem. Mater.*, 1997, **9**, 2448–2458.
59 J. Rodriguez-Mirasol, T. Cordero, L. R. Radovic and J. J. Rodriguez, *Chem. Mater.*, 1998, **10**, 550–558.
60 J. S. Lee, A. Hirao and S. Nakahama, *Macromolecules*, 1988, **21**, 274–276.
61 M. Templin, A. Franck, A. Du Chesne, H. Leist, Y. Zhang, R. Ulrich, V. Schädler and U. Wiesner, *Science*, 1997, **278**, 1795–1798.
62 Y. Zhai, Y. Dou, X. Liu, B. Tu and D. Zhao, *J. Mater. Chem.*, 2009, **19**, 3292–3300.
63 P. F. Fulvio, R. T. Mayes, X. Wang, S. M. Mahurin, J. C. Bauer, V. Presser, J. McDonough, Y. Gogotsi and S. Dai, *Adv. Funct. Mater.*, 2011, **21**, 2208–2215.
64 K. Wieczorek-Ciurowa and A. J. Kozak, *J. Therm. Anal. Calorim.*, 1999, **58**, 647–651.
65 E. P. Sajitha, V. Prasad, S. V. Subramanyam, S. Eto, K. Takai and T. Enoki, *Carbon*, 2004, **42**, 2815–2820.
66 L.-S. Zhong, J.-S. Hu, A.-M. Cao, Q. Liu, W.-G. Song and L.-J. Wan, *Chem. Mater.*, 2007, **19**, 1648–1655.
67 S. Lagergren, *K. Sven. Vetenskapsakad. Handl.*, 1898, **24**, 1–39.
68 Y. S. Ho, G. McKay, D. A. J. Wase and C. F. Forster, *Adsorpt. Sci. Technol.*, 2000, **18**, 639–650.
69 R.-S. Juang and M.-L. Chen, *Ind. Eng. Chem. Res.*, 1997, **36**, 813–820.
70 Kinetics of Reaction in Pure and Mixed Systems, in *Soil Physical Chemistry*, ed. D. L. Sparks, CRC press, Boca Raton, 1986.
71 S. K. Srivastava, R. Tyagi and N. Pant, *Water Res.*, 1989, **23**, 1161–1165.
72 Y. Li, B. Gao, T. Wu, D. Sun, X. Li, B. Wang and F. Lu, *Water Res.*, 2009, **43**, 3067–3075.
73 N. Ahmed El, *J. Hazard. Mater.*, 2009, **161**, 132–141.
74 A. El-Sikaily, A. E. Nemr, A. Khaled and O. Abdelwehab, *J. Hazard. Mater.*, 2007, **148**, 216–228.
75 U. K. Garg, M. P. Kaur, V. K. Garg and D. Sud, *J. Hazard. Mater.*, 2007, **140**, 60–68.
76 L. S. Zhong, J. S. Hu, H. P. Liang, A. M. Cao, W. G. Song and L. J. Wan, *Adv. Mater.*, 2006, **18**, 2426–2431.
77 B. M. Weckhuysen and I. E. Wachs, *Chem. Rev.*, 1996, **96**, 3327–3349.
78 D. V. Dimitrov, G. C. Hadjipanayis, V. Papaefthymiou and A. Simopoulos, *J. Vac. Sci. Technol., A*, 1997, **15**, 1473–1477.
79 X.-M. Liu, S.-Y. Fu, H.-M. Xiao and C.-J. Huang, *J. Solid State Chem.*, 2005, **178**, 2798–2803.
80 B. R. V. Narasimhan, S. Prabhakar, P. Manohar and F. D. Gnanam, *Mater. Lett.*, 2002, **52**, 295–300.
81 B. D. Cullity and C. D. Graham, *Introduction to Magnetic Materials*, John Wiley & Sons, Hoboken, New Jersey, 2nd edn, 2009, p. 531.
82 H. Jabeen, V. Chandra, S. Jung, J. W. Lee, K. S. Kim and S. B. Kim, *Nanoscale*, 2011, **3**, 3583–3585.
83 N. Melitas, O. Chuffe-Moscoso and J. Farrell, *Environ. Sci. Technol.*, 2001, **35**, 3948–3953.
84 S. B. Lalvani, T. Wiltowski, A. Hübner, A. Weston and N. Mandich, *Carbon*, 1998, **36**, 1219–1226.
85 L. Dupont and E. Guillon, *Environ. Sci. Technol.*, 2003, **37**, 4235–4241.